Volume 15 | Number 6 | 14 February 2019 | Pages 1067–1458

Soft Matter

rsc.li/soft-matter-journal

ISSN 1744-6848

ROYAL SOCIETY OF CHEMISTRY | Celebrating IYPT 2019

PAPER

Lucia Stein-Montalvo, Douglas P. Holmes *et al.*

Buckling of geometrically confined shells

Soft Matter

PAPER

View Article Online
View Journal | View Issue

Cite this: *Soft Matter*, 2019, **15**, 1215

Buckling of geometrically confined shells†

Lucia Stein-Montalvo, *[a] Paul Costa,[b] Matteo Pezzulla [ac] and Douglas P. Holmes *[a]

Received 6th October 2018,
Accepted 4th December 2018

DOI: 10.1039/c8sm02035c

rsc.li/soft-matter-journal

We study the periodic buckling patterns that emerge when elastic shells are subjected to geometric confinement. Residual swelling provides access to range of shapes (saddles, rolled sheets, cylinders, and spherical sections) which vary in their extrinsic and intrinsic curvatures. Our experimental and numerical data show that when these moderately thick structures are radially confined, a single geometric parameter – the ratio of the total shell radius to the amount of unconstrained material – predicts the number of lobes formed. We present a model that interprets this scaling as the competition between radial and circumferential bending. Next, we show that reducing the transverse confinement of saddles causes the lobe number to decrease with a similar scaling analysis. Hence, one geometric parameter captures the wave number through a wide range of radial and transverse confinement, connecting the shell shape to the shape of the boundary that confines it. We expect these results to be relevant for an expanse of shell shapes, and thus applicable to the design of shape-shifting materials and the swelling and growth of soft structures.

Shells are notorious for their nonlinear response to mechanical loading, and subtle changes to how they are held, or constrained, can have profound affects on how they deform. Confinement of soft shells can induce dramatic deformations as illustrated in Fig. 1, where radial confinement is increased from left to right. These mechanics are relevant to soft biological tissues, as their morphology often depends on a combination of mechanical forces imparted along their boundaries, and non-mechanical forces that drive growth or swelling. Confinement of soft tissues can result in the wrinkling and scar formation of surgical wounds,[1] and these changes in shape or morphology are not purely cosmetic. For example, during the embryogenesis of the ciliary body of an avian eye, differential growth induces wrinkles that radiate outward from the retina,[2] a stiff region that resists deformation. Capillary blood vessels form in the valleys of these wrinkles, while molecules that promote neural cell adhesion fail to express in the regions where these epithelial tissues wrinkle.[3,4] These effects are entirely mechanical, as evidenced by experiments that induced wrinkles in the chick eyes by swelling them in ethanol.[2,4] Similar studies on the differential swelling and growth of artificial tumors[5,6] and biofilms[7,8] described the role of confinement and the mechanics of these circumferential wrinkles in much greater detail. Radial confinement occurring within airways and arteries,[9] as seen in buckling and folding of mucous membranes, can cause the collapse or closure of the oesophagus,[10] blood vessels,[11] and gastrointestinal tract.[12]

Beyond these biological systems, the ability to prescribe and control the shape of objects has ushered in an age of designer materials.[13] By dictating the volumetric strain in specific regions of soft elastomers, researchers have been able to morph 2D sheets into 3D shells,[14–16] with features spanning multiple length scales.[17,18] Differential swelling, sometimes accomplished by using the residual polymer chains left in portions of cured elastomers, has been used to fabricate helical ribbons,[19] rolled sheets,[20] saddles,[21] pinched spheres,[22] and wavy strips and discs.[23–25] Even for free, unconstrained plates and shells the shape selection process is non-trivial. The shapes that result from differential swelling can be determined by examining how swelling alters the metric tensor of the middle surface of the plate, an approach described by the so-called theory of unconstrained non-Euclidean plates.[26] When swelling only imparts a local curvature change along the middle surface, as is the case for the residual swelling of bilayer plates and shells, the non-mechanical swelling process can be cast as a mechanical stimulus which alters the natural curvature of the shell,[22] and the stability of these structures can be evaluated using techniques common to applied mechanics. The inverse problem – knowing a desired shape and searching for the correct initial conditions necessary to achieve it – is a problem that has received far less attention, but will likely be more desirable.

---

[a] *Department of Mechanical Engineering, Boston University, Boston, MA, 02215, USA. E-mail: lsmontal@bu.edu, dpholmes@bu.edu*
[b] *École Polytechnique, 91128 Palaiseau, France*
[c] *Institute of Mechanical Engineering, École Polytechnique Fèdèrale de Lausanne, 1015 Lausanne, Switzerland*

† Electronic supplementary information (ESI) available. See DOI: 10.1039/c8sm02035c

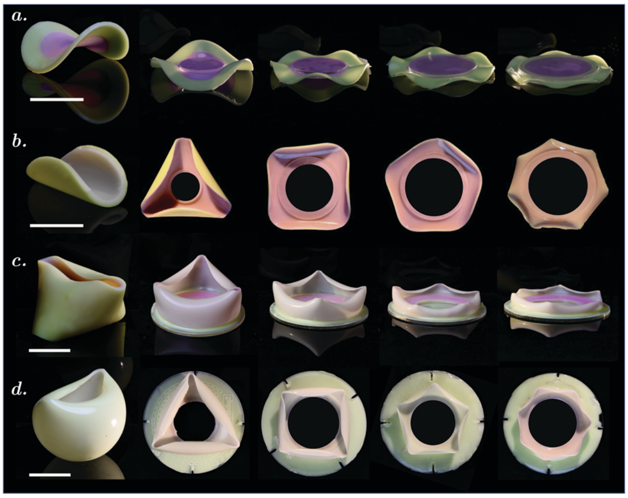

Fig. 1 As the extent of confinement increases from left to right, the (a) saddle, (b) rolled sheet, (c) cylinder and (d) spherical segment exhibit more lobes. In (a and b), shells are clamped between acrylic plates of increasing diameter. The cylinder and sphere cut to varied (c) heights and (d) latitudes, and fixed with an acrylic ring at the base. Shells are made of polyvinylsiloxane (PVS). Scale bars represent 30 mm.

Work by Dias *et al.* demonstrated how to find the metric for a variety of axisymmetric shapes,[27] while more recent work has shown how to find the metric for a wide range of shapes, including a human face, when a curvature can be prescribed at any point.[28]

In the effort to understand and control shape change in soft and thin structures, the interplay between intrinsic geometry and geometric constraints is still not well understood. Confining a simple 1D object, *i.e.* an elastica, within a rectangular box is a nontrivial problem, in part due to the unknown and evolving location of the point of contact between the elastica and the walls.[29–33] Similar problems emerge in the packing of thin sheets, for instance pushing a plate through a ring causes it to form a developable cone, or d-cone,[34–39] and in the confinement of a thin plate between two hemispheres[40] or onto a droplet of water.[41] Confinement of intrinsically curved shells has received less attention, with an exception being the behavior of shells under indentation,[42] including a hybrid experimental-numerical study of the response of positively curved shells to indenters of varied geometries.[43] In this work, we present a primarily experimental study on how geometric confinement facilitates pattern formation in structures with intrinsic curvature. We consider shells with various mean and Gaussian curvatures under a range of radial confinement, and we examine the combined role of radial and transverse confinement on negatively curved shells, or saddles. We focus our study on four categories of shapes, shown in Fig. 1 and schematically in Fig. 2a: saddles, rolled sheets, cylinders, and spherical segments. Each is initially axisymmetric and exhibits periodic postbuckling patterns when subjected to geometric constraints. These geometries were chosen to access a range of average Gaussian and mean curvatures in their reference $\left(\mathring{\mathscr{K}}_{\mathrm{avg}}, \mathring{\mathscr{H}}_{\mathrm{avg}}\right)$ and deformed $(\mathscr{K}_{\mathrm{avg}}, \mathscr{H}_{\mathrm{avg}})$ configurations.

The range of structures studied is outlined in Fig. 2b. Of the four shapes we study, two start out as flat plates – one of these changes its average mean curvature, and the other changes its average Gaussian curvature after fabrication. Our study omits spherical caps, which have been well-characterized, *e.g.* in ref. 43. These shells are relatively thick as compared to recent work on thin film confinement,[41,44,45] and we will show that the characteristic pattern of deformation can be described by a single geometric parameter that appears to be independent of shell thickness in this regime.

1 Radial confinement

Each of the unconstrained, residually stressed shapes are shown in the leftmost column of Fig. 1. We begin by constraining the rolled sheets and saddles in the radial direction by clamping the shells between two rigid acrylic sheets of radius R_{c}. In Fig. 1a & b, we increase R_{c} from left to right while keeping the shell radius R and thickness h constant, and we see that the number of lobes N, or wavenumber, increases. Three-dimensional simulations were implemented in COMSOL Multiphysics to validate these experiments for the three bilayer geometries (rolled sheets, cylinders, and spheres). Residual swelling is represented by an inelastic distortion field, and Dirichlet boundary conditions around a ring of radius R_{c} act as the external constraint (see Appendix A for details on fabrication and simulations).

The wavenumber appears to be insensitive to changes in thickness in the range of h/R we considered (Fig. 3a), $h/R \in [0.008, 0.13]$ – thicker shells behave more like 3D bodies, while thinner shells made from these materials (see Appendix) deform significantly under gravity. Instead, it appears that the wavenumber is inversely proportional to the length of material that is unconstrained, *i.e.* $r \equiv R - R_{\mathrm{c}}$.

The bending energy of the shell, which we assume to be decoupled from the stretching energy, is known to scale as $\mathscr{U}_{\mathrm{b}} \sim \frac{B}{2}\int \rho^2 \mathrm{d}\omega$. The quantity $\rho = (\kappa - \kappa_{\mathrm{o}})$ represents the

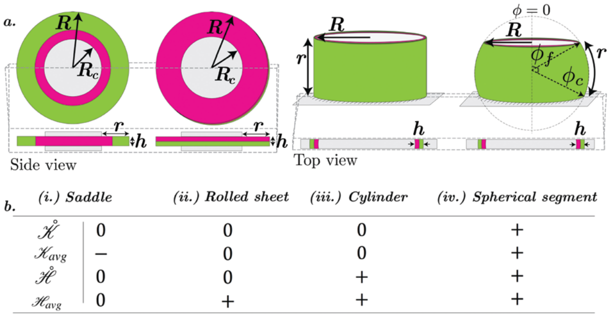

	(i.) Saddle	*(ii.) Rolled sheet*	*(iii.) Cylinder*	*(iv.) Spherical segment*
$\mathring{\mathscr{K}}$	0	0	0	+
$\mathscr{K}_{avg}$	–	0	0	+
$\mathring{\mathscr{H}}$	0	0	+	+
$\mathscr{H}_{avg}$	0	+	+	+

Fig. 2 (a) Schematics showing pre-residual swelling configurations and relevant geometric parameters for the (i) saddle, (ii) rolled sheet, (iii) cylinder, and (iv) spherical segment. Pink areas will "shrink" while green ones will "grow" upon residual swelling, and grey represents areas constrained by acrylic plates. (b) Table displays initial (accented "o") and post-swelling (subscripted "*avg*") Gaussian $\mathscr{K}$ and $\mathscr{H}$ mean curvatures for each shape.

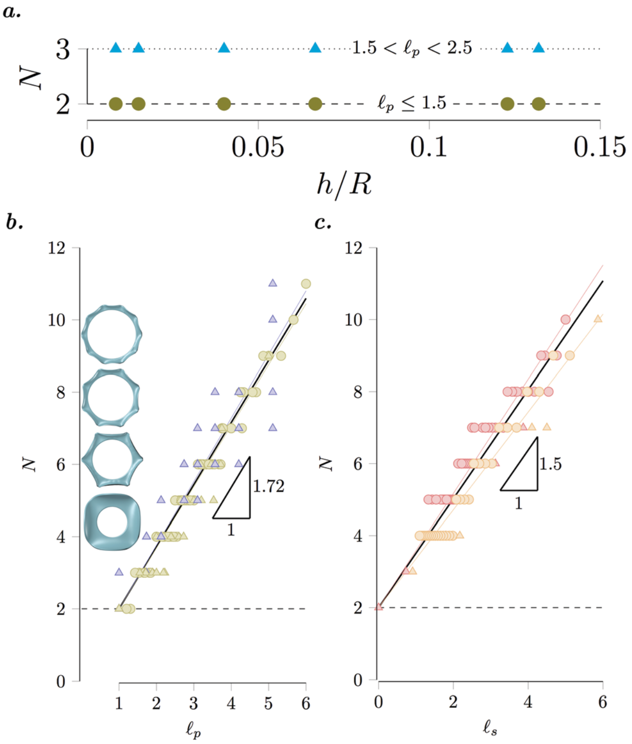

Fig. 3 (a) In the thickness range we study, the wavenumber is insensitive to changes in thickness, h. Instead, the amount of unconstrained material, quantified by ℓ, sets the wavenumber: for ℓ_p in a fixed range, but h/R varied, N (shown for rolled sheets) is unaffected. (b & c) The number of lobes N may be reduced to one geometric parameter, $\ell = R/r$, which quantifies the relative amount of constraint. The evolution of N is a linear function of ℓ. Triangles are experimental data points and circles are from simulations. Solid lines of best fit, and their slopes, are shown in each plot. Free of constraints, each shape has two lobes (dotted line). Solid horizontal axes are drawn according to the minimum value for ℓ. (b) For saddles (purple) and rolled sheets (green), $\ell_p = R/(R - R_c)$, and $\min(\ell_p) = 1$. Inset: Results from simulations for rolled sheets for (bottom to top) $\ell_p = \{2.2, 3.2, 4.5, 5.8\}$. (c) For cylindrical shells (red) with height r, $\ell_s = R/r$. For spherical segments (orange), $\ell_s = \sin\phi_f/(\phi_c - \phi_f)$. The minimum of ℓ_s is 0.

curvature strains – the difference between the deformed curvature κ and the curvature in the reference (unconstrained) state κ_o – and dω is the area element.

The bending energy penalizes high curvatures, so in the circumferential direction, long wavelengths are preferable. We assume that the θ-direction wrinkle curvature will scale with the amplitude and wavelength as $\kappa^{(\theta)} \sim A/\lambda^2$, so $\rho^{(\theta)} \sim ((A/\lambda^2) - (A_o/\lambda_o{}^2))$. When the two initial lobes, each of amplitude A_o, are split into N lobes, the amplitude becomes $A = 2A_o/N$ – the total length does not change. Thus, $A_o \sim NA$. Similarly, $\lambda = 2\pi R/N \Rightarrow N \sim R/\lambda$, and $\lambda_o \sim R$, so that $\varrho^{(\theta)} \sim A/\lambda^2 - A/(\lambda R)$. Again by inextensibility, $\lambda \sim A$, so we can also say $\rho^{(\theta)} \sim 1/\lambda - 1/R$. Together, this gives

$$\mathscr{U}_{\mathrm{b}}^{(\theta)} \sim \frac{B}{2}\int\left(\frac{1}{\lambda}-\frac{1}{R}\right)^2 \mathrm{d}\omega. \tag{1}$$

The question in regard to these constrained shells is: what opposes the circumferential bending energy to produce shorter wavelengths? Typically in (unconstrained) shell problems, competition between bending and stretching drives deformation. However, stress distributions of similarly confined structures obtained experimentally[23] and numerically[46] suggest that stretching in the radial direction is concentrated in a small region near the inner boundary. Further, since in this thickness regime the shell thickness does not appear to play a dominant role in setting the wavelength, or wavenumber (Fig. 3a), of these constrained shells, we expect that any energy comparison should be independent of thickness to leading order. Thus, we hypothesize that bending in the radial direction is the other relevant contribution to the energy:‡ along the length r, the radial bending energy prefers short wavelengths (smaller amplitudes).

In the radial direction, the curvature $\kappa^{(r)} \sim A/r^2$, so we can say $\rho^{(r)} \sim (\kappa^{(r)} - \kappa_o^{(r)}) \sim A/r^2 - A_o/R^2$. With the same arguments as before applied to the numerator, the bending energy in the radial direction is given by

$$\mathscr{U}_{\mathrm{b}}^{(r)} \sim \frac{B}{2}\int\left(\frac{\lambda}{r^2}-\frac{1}{R}\right)^2 \mathrm{d}\omega. \tag{2}$$

Balancing the two energies in (1) and (2) gives $\lambda \sim r$. With $\lambda = 2\pi R/N \sim R/N$, and defining $\ell \equiv R/r$, we arrive at a scaling of the wavenumber as a function of the unconstrained, or free length of the shell:

$$N \sim \ell. \tag{3}$$

In Fig. 3b, we plot experimentally and numerically obtained wavenumbers N as a function ℓ_p, which is ℓ for the shells that initially started as flat plates. When the constraint $R_c \rightarrow 0$ the dimensionless length $\ell_p \rightarrow 1$, and experiments on unconstrained shells confirm that $N \rightarrow 2$ (Fig. 1), suggesting that for rolled sheets and saddles eqn (3) should be modified to $N \sim \ell_p + 1$. This scaling is plotted as a solid line on Fig. 3b, with a slope of 1.72 found *via* linear regression. We would expect the slope to be of $\mathscr{O}(1)$ if the scaling is valid, and these results suggest that our approximations were reasonable.

We now turn our attention to shells with initially nonzero mean and Gaussian curvatures. Physically, the scaling from eqn (3) suggests that the wavenumber will increase linearly as the free, unconstrained length of the shell decreases. For the cylinders and spherical segments constrained at their base, the free length that decreases from left to right on Fig. 1c & d is the arclength r of material from the clamped base to the shell opening, and similar to the rolled sheets and saddles, as this free length is decreased the wavenumber increases. Therefore, we anticipate that eqn (3) will also capture the wavenumber of these constrained shells, provided the appropriate limits on N and ℓ_s are met, where ℓ_s is ℓ for shells that have are initially curved. Here, the unconstrained shell corresponds to $r \rightarrow \infty$,

---

‡ Inherently, these assumptions are contradictory – bending in both directions throughout the free area implies stretching, which we have chosen to neglect. We anticipate that a more thorough analysis is needed to relieve this contradiction. Here, we assume these stretching effects are small compared to bending. We are grateful to James Hanna who provided helpful insight to clarify this scaling.

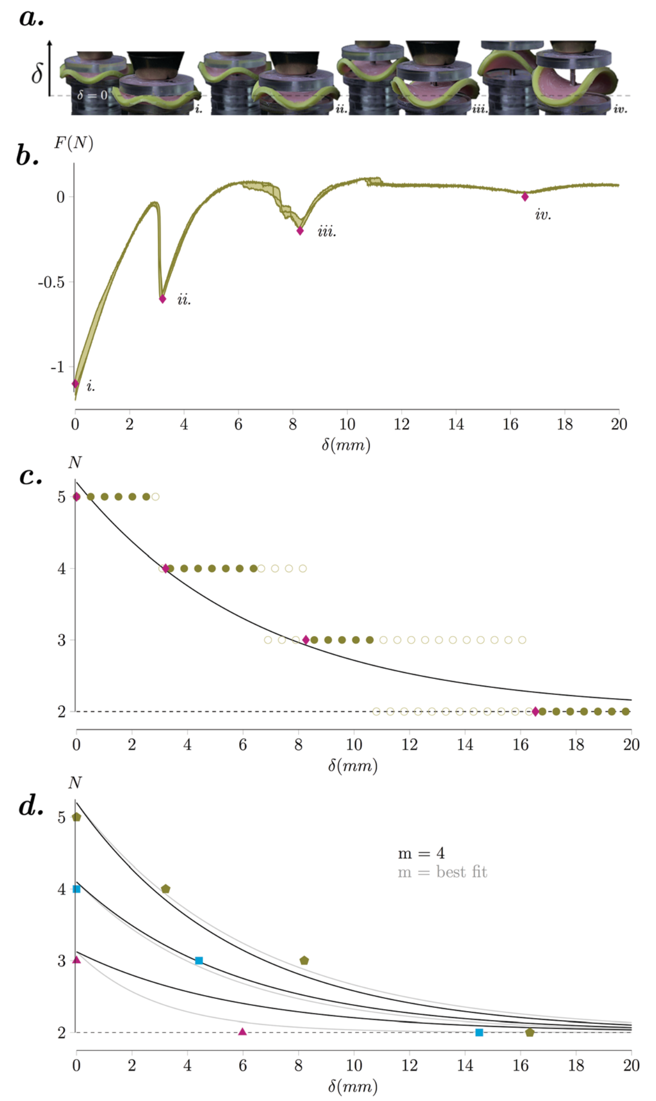

Fig. 4 (a) As δ increases from left to right, the number of lobes (N) decreases. The recessed images are mirrored views showing the back side of saddles. (b) Force–displacement curves of three displacement-controlled tests on a single shell. Pink diamonds correspond to lobe transition points with Roman numerals indicating the transition from five (i), to four (ii), to three (iii) to two (iv) lobes. (c) Wavenumber N *vs.* δ for the same sample. Solid points correspond to symmetric lobes, and open circles correspond to transitions between lobes. We expect the solid theoretical curve to capture the points marked by pink diamonds. This curve is eqn (5) with $m = 3.5$. (d) The same equation captures experimental lobe switches (points, as in c) with different geometric parameters. Black curves fix $m = 4$, and grey curves correspond to best fit m values: from top, $m = 3.68$, $m = 4.38$, $m = 8.00$.

or $\ell_s \rightarrow 0$, which is analogous to the two lobe deformation (*i.e.* $N \rightarrow 2$) observed with a "pinch in a pipe".[47] This suggests that for cylinders and spherical segments, we expect that eqn (3) should be modified to $N \sim \ell_s + 2$. In Fig. 3c, we plot experimentally and numerically obtained wavenumbers N as a function ℓ_s for cylinders and spherical segments. The scaling $N \sim \ell_s + 2$ is plotted on Fig. 3c, with a slope of 1.50 found *via* linear regression. These results seem to be in good agreement with this reduced order model, suggesting that the wavenumber of a wide range of constrained shells can be characterized with a dimensionless parameter corresponding to the free length of the shell.

2 Transverse confinement

We will now relax the radial confinement to investigate shell behavior under varying amounts of transverse confinement. We focus primarily on an experimental analysis of saddles, because to our knowledge there are only limited examples of the transverse confinement of saddles in the literature, and the experiments on saddles are the most practically feasible out of the structures discussed in Section 1. We constrain the shells in the transverse direction with quasi-static, displacement-controlled tests in which a saddle is compressed between pairs of acrylic plates of radius R_c. Initially, the distance d between the top and bottom plates equals the saddle's thickness, *i.e.* $\delta = d - h = 0$ (Fig. 4a & b, (i)), which represents the limit discussed in Section 1.

As we separate the distance between the two plates by an amount δ, there is a non-monotonic decrease in the applied compressive load, and the number of lobes decreases, as shown in Fig. 4a (a more detailed experimental protocol is discussed in Appendix A.2, and a video may be found in the ESI†). The decrease in the compressive load is nearly linear for $\delta/A \ll 1$, and then reaches a minimum when one point of contact between the acrylic plate and the saddle is lost, thus beginning the mode shape transition from $N = N_{\max}$ to $N - 1$ lobes. The load immediately increases, and once the saddle has reaches $N - 1$ (asymmetric) lobes (Fig. 4a & b, (ii)) the load once again decreases. When a new symmetric shape is reached at $N - 1$ lobes, the slope of the force–displacement curve decreases but remains positive, and the process repeats until $\delta \simeq A$, $F \simeq 0$, and there are $N = 2$ lobes (Fig. 4a & b, (iv)). The slope of the force–displacement curves through these transitions appears to gradually decrease, pointing to a diminishing effective stiffness as δ increases. Fig. 4b shows these trends in a force–displacement curve for a representative sample that achieves a maximum of 5 lobes at $\delta = 0$.

We now aim to provide some mechanistic insight as to the lobe transitions from $N_{\max}$ to $N = 2$ for saddles as the transverse constraint is reduced. Here, we know the two limits: (1) as $\delta \rightarrow \infty$ we expect that $N \rightarrow 2$, and (2) as $\delta \rightarrow 0$ we expect that $N \rightarrow N_{\max}$ as given by eqn (3). The first limit can be simplified, because the sheet will be unconstrained once δ is larger than the amplitude of the shell's lobes, *i.e.* $N \rightarrow 2$ when $\delta \geq A$. In these experiments, while in principle ℓ_p is fixed, in effect the free length of the shell may be approximated as being a function of δ, *i.e.* $r_\delta(\delta)$, with $r_\delta(0) = r$ from Section 1. As an *ansatz* for r_δ that meets these two limits, we chose a logistic function in the form

$$r_\delta(\delta) = \frac{R}{1 + \frac{R_c}{r} e^{-m\frac{\delta}{A}}}, \qquad (4)$$

where m is an unknown constant that describes how quickly the unconstrained length will transition between r and R.

Substituting this *ansatz* into equations $\mathscr{U}_\mathrm{b}$ and $\mathscr{U}_\mathrm{k}$ for r, we can solve for $N(\delta)$. Following some algebra, we find

$$N(\delta) \sim \ell_\mathrm{p} + 1 - \frac{R_\mathrm{c}}{r}\left(1 - \mathrm{e}^{-m\frac{\delta}{A}}\right). \tag{5}$$

which reduces to eqn (3) for plates when $\delta = 0$. In Fig. 4c, we plot the experimentally observed wavenumber as a function of δ. The transition process is highly nonlinear, and so we note the transition between two wavenumbers with open symbols, while highlighting the transition points from the local minima in the force–displacement curve as filled diamonds. Eqn (5) is plotted as a solid black curve, with $m = 3.5$ chosen as a best fit parameter to the transition points. Although m is effectively a fitting parameter, we anticipate that it will depend on the bending rigidity of the saddle. We have not taken into account how the magnitude of the saddle's Gaussian curvature, which will be related to the amplitude of the lobes, nor the shell thickness affect the transition points, however we expect that m will be a function of these parameters. Further testing, in particular numerics, will help explain the contribution of $\mathscr{K}$ and h to the transition between mode numbers. Still, we note that for the samples we tests, using $m = 4$ captures the transition points for shells with $N_\mathrm{max} = 5$, $N_\mathrm{max} = 4$, and $N_\mathrm{max} = 3$ (Fig. 4d). Choosing the best fit values of m for each sample ($m = 3.7$, $m = 4.4$, and $m = 8.0$) changes the critical δ for observing lobe transitions, but qualitatively provides similar values. In general, the form of (5) clarifies the relative contributions of transverse (δ) and radial (R_c) confinement. At low δ values, radial effects dominate. As the wave number depends on δ exponentially, however, the effects of reduced transverse confinement quickly take over with increasing δ.

3 Conclusions

In this work, we explored geometry's fundamental role in the periodic buckling patterns that emerge in confined shells. We studied shells covering a range of Gaussian and mean curvatures, accessible *via* residual swelling. We first saw that one simple geometric parameter, ℓ, which relates the overall shell radius to the amount of unconfined material, predicts the number of wrinkles (N) a radially confined shell will adopt. Then for negatively curved saddles, we reduced the radial constraint by varying transverse confinement and measured the transition points between wavenumbers.

We observed that decreasing the amount of confinement, whether in-the-plane or vertically, makes bending in the circumferential direction costly – lower buckling modes are energetically preferable in a low-confinement regime. This interpretation allowed us to generalize ℓ to include our range of transverse confinement. Thus, the model given by relation (5) captures a wide range of bidirectional confinement.

There is much to be done in terms of more rigorously understanding why thickness and stretching appear to be unimportant, and to put our scaling assumptions on firmer ground. A nice analog to our transverse confinement of saddles is the transverse confinement of an elastica.[31,32] In these works, solutions for the confined elastica[29,30] are extended to thin plates constrained progressively in the vertical direction. Our problem has subtle differences, notably that our shells are naturally curved, and our confining plates are smaller than the shell size. However, the transitions between buckling modes in our experiments are reminiscent of these studies, including qualitative features like planar contact, free-standing folds, and rolling.[33] These parallels suggest a way to pursue a more formal connection between the two problems. The shells studied in this work are residually stressed, and the magnitude of residual stress did not enter our mechanical model. It was recently shown that the magnitude of residual stress in shells will alter the critical point at which an instability occurs, *i.e.* the load required to buckle the structures, but that the instability remains qualitatively similar.[48] Also, as others[43] have observed, contact plays an important role in transverse confinement. Further numerical analysis of these constrained shells would be beneficial, in particular, such an analyses could also offer a more geometric freedom, with regards to both shells and their confining boundaries, beyond what is readily accessible experimentally. In general, we anticipate these results will aid in the design of shape-shifting structures, and we believe there are many open questions regarding the role of confinement when designing structures that change shape on command.

Conflicts of interest

There are no conflicts to declare.

Appendix A

A.1 Structure fabrication

To fabricate the shapes shown in Fig. 1, we use a technique known as residual swelling.[20,21] We use two polyvinylsiloxane (PVS) elastomers, which we will refer to as green (Zhermack Elite Double 32, $E = 0.96$ MPa) and pink (Zhermack Elite Double 8, $E = 0.23$ MPa). The materials are cast in as fluids and allowed to thermally crosslink, or cure, at room temperature for 20 minutes. After curing, the pink elastomer has residual polymer chains within the material, and these residual free chains flow into the green elastomer when the two materials are in contact with each other. The local loss of mass causes the pink material to decrease in volume, or shrink, while the green material correspondingly swells, thus inducing a differential swelling in the structure which preserves its total mass. Differential swelling in shells can lead to residually stressed structures that emerge because the shell must deform to accommodate a geometric incompatibility.[49] When the differential swelling occurs through the shell's thickness, it deforms in a nearly isometric manner in the bulk of the shell, away from shell's edges,[22] and when the differential swelling occurs in-the-plane of the shell the deformation is dominated by stretching.[21] These opposing deformations explain why the initially flat shapes can be morphed into either rolled sheets or saddles. As residual swelling is a diffusive process, the time to deform scales with the square of the dimension across which swelling occurs. This characteristic dimension for swelling is either the thickness $h \approx 1$ mm, or in the case of saddles, where residual swelling occurs in-the-plane, the radius, $R = 30$ mm.[21]

To make homogeneous rolled sheets, we use a spin coater (Laurel Technologies, WS-650-23) to deposit a pink layer of PVS atop a laser-cut (Epilog Laser Helix, 75 W) circular acrylic plate, $R \in [25\text{ mm}, 35\text{ mm}]$. After it cures, we add a green layer in the same manner. The residual swelling first bends the sheet into a shallow spherical cap, and then ultimately buckles it into a rolled sheet – a cylinder-like shape that is open along its directrix. The rolled sheet is nearly isometric away from its edges (*i.e.* $K_{\text{avg}} = 0$) and its non-zero mean curvature is linearly proportional to the natural curvature imposed by residual swelling.[20,22,50] In the range of thicknesses we study, the unconstrained mean curvature $\mathscr{H}$ seems to have no effect on the wavenumber. Qualitatively, we observe that higher $\mathscr{H}$ does, however, increase the amplitude of wrinkles in constrained shells.

Saddles are made by laser-cutting a negative circular mold ($R = 30$ mm) from clear cast acrylic sheets of thickness h: 0.794 mm ± 0.119 mm (inventables), 1.589 mm (tolerance −0.584 mm to +0.254 mm), 2.381 mm (−0.034 mm to +0.025 mm), or 3.175 mm (−0.635 mm to +0.381 mm) (McMaster-Carr). This circular mold is glued atop a base acrylic plate, and a smaller circle, radius $R_c \in \{12.5\text{ mm}, 28.25\text{ mm}\}$, is centered and fixed to the base plate. We then pour green PVS to form a ring, filling the mold up to the acrylic sheet thickness. After the ring cures, the smaller circle is removed and the remainder is filled with pink PVS. After residual swelling, a saddle shape forms: $\mathscr{H}_{\text{avg}} \approx 0$ and $\mathscr{K}_{\text{avg}} < 0$ – the value of the latter depends on the ratio of pink to green polymer.[20] In-plane swelling is quite a bit slower than through-thickness swelling, since the characteristic length scale changes from the thickness to the radius.[21] The dynamics can be increased by extracting the free polymer chains in a solvent bath, *e.g.* ethyl acetate.

Cylinders and spherical segments are poured as bilayers over corresponding 3D molds. Spherical segments are formed by coating a metal ball-bearing with viscous PVS so that each layer has approximately uniform thickness.[22,51] These spherical shells have positive average mean and Gaussian curvatures both before and after the swelling process. Cylinders are fabricated similarly[52] (see Fig. 5), and like spheres, the initial mean curvature $\mathring{\mathscr{H}} > 0$, though $\mathring{\mathscr{K}} = 0$. After deformation, a "pinched pipe" forms,[47] with $\mathscr{H}_{\text{avg}} > 0$ and $\mathscr{K}_{\text{avg}} > 0$.

For the experiments described in Section 1, rolled sheets and saddles are clamped in the center between two laser-cut acrylic plates of equal size, $R_c \in \{12.7\text{ mm}, 30.5\text{ mm}\}$. Cylinders and spherical segments, on the other hand, are constrained by acrylic plates glued to the base with a very thin layer of green VPS. Cylinders are then cut to varied heights, and spheres are cut at different latitudes: the angle ϕ_f is subtended by the arclength from the origin (the north pole) to the top cut (the free surface). The base, where the shell is constrained, is defined by the angle ϕ_c. Schematics of the pre-swelling configurations, including constraints, are given in Fig. 2. Thickness is measured at $h = \{0.25, 0.45, 0.75, 1.5, 4\}$ mm ± 0.15 mm for Section 1, and $h \in [2.381\text{ mm} \pm 0.1\text{ mm}, 3.175\text{ mm} \pm 0.1\text{ mm}]$ for the saddles discussed in Section 2.

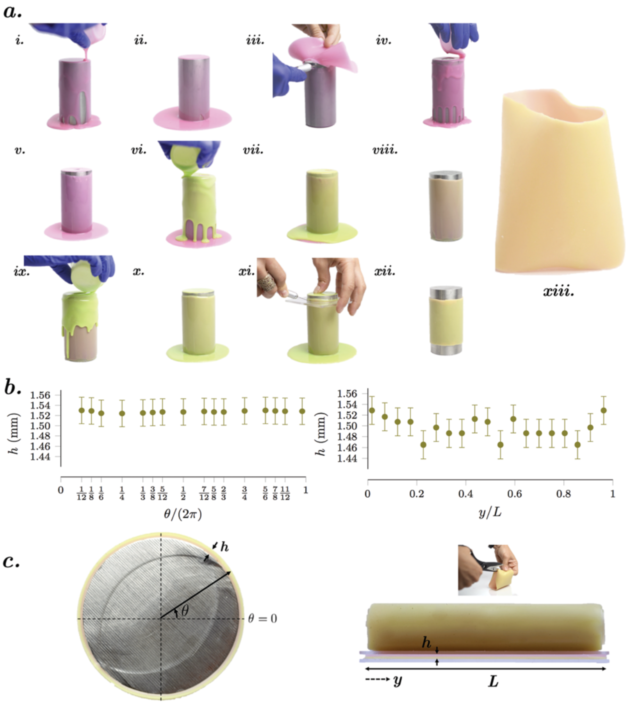

Fig. 5 (a) Fabrication process for a bilayer cylinder: (i and ii) the first pink layer of PVS is poured to uniformly coat the steel cylinder. (iii) After 20 minutes, the first layer has cured. The cylinder is flipped upside-down, and the excess material is removed. (iv and v) A second layer of pink PVS is poured in order to achieve a uniform thickness in the vertical direction. (vi and vii) After another 20 minutes, both pink layers have cured. A green layer is added in the same manner. (viii) After 20 minutes, the excess material is removed and the cylinder is flipped upside-down again. (ix and x) The final green layer is added. (xi and xii) After the final layer has cured (20 minutes), the bilayer cylinder is cut from the mold using a straightedge. (xiii) The bilayer cylinder once peeled from the mold. Residual swelling causes the cylinder to buckle into a "pinched pipe". (b) Thickness *versus* (right) axial and (left) azimuthal ($y = 0$) position, corresponding to parameters shown in the images in (c). Thickness is relatively uniform in both directions, albeit more so in the radial direction. Measurements were taken using ImageJ. (c) Top view (left) and cut view (right) show parameters relevant to the above plots. Right: To obtain thickness measurements in the axial direction, the cylinder is cut, then glued between glass plates to prevent rolling.

The wavenumber in rolled sheets, cylinders, and spheres is indifferent to whether the constraint is applied before or after residual swelling occurs, and the experimental data in Fig. 1b & c represents a mix of both scenarios.

For saddles, where the swelling gradient lies in-the-plane, the confining plates are added after the swelling process. Our aim in this paper was to examine how, given a saddle, constraints affect its shape. Therefore, residual swelling is a tool to make these saddles. Applying the constraint beforehand leads to a different question: how does confinement affect saddle formation in residual swelling?

If the radius of the pink PVS region $R_p < R_c$, the clamp forces the pink region to stretch to conform to R_c. The inner perimeter of the green region is fixed, but the outer perimeter decreases as free chains are lost from the green polymer. Then, instead of buckling into a negatively curved saddle, the shape develops positive Gaussian curvature. This is analogous to ref. 21, in which structures comprised of geometrically mismatched disks and annuli buckle into saddles if the perimeters require that the annulus stretches, and domes if the annulus must compress.

A.2 Mechanical force testing

The saddles used in Section 2 were fabricated with a centered 2.25 mm radius hole through which we guide a 2 mm radius rod as transverse confinement is varied. We determined this hole to be necessary for maintaining the saddle's position but negligible for our purposes – it has no effect on lobe number. Care was taken to align shells as close to centered as possible, as shells are sensitive to initial conditions (see ESI†).

We investigate transverse confinement with a setup designed for the INSTRON 5943. We attach a drill-type grip (Instron 0.375 in Keyless Drill-Type Chuck Assembly) to the load cell to secure an aluminum rod (2 mm radius), which is screwed to an internally threaded acrylic plate of radius R_c. A second partially threaded rod is attached to the underside of this top plate, pointing downward. The rod is guided through the saddle's center hole and then through a hole also of radius 2.25 mm in the center of the acrylic base plate, which itself has radius R_c. The base plate is affixed to a thick tube of outer radius $< R_c$, inner radius 3.5 mm and height 44.45 mm. This tube is comprised of stacked acrylic rings each of thickness 6.35 mm, glued together and closed at the base. The base of the tube is screwed to a tapped optical table.

Displacement-controlled tension tests are performed at a rate of 4 mm min^{-1} and force is measured with a 500 N load cell (resolution 0.0025 N). Videos were taken with a Nikon D610 DSLR Camera and were used for post-processing in conjunction with Instron data.

A.3 Numerics

For the three bilayer geometries where residual swelling occurs through-the-thickness, we sought to validate the experiments from Section 1 with simulations developed in COMSOL Multiphysics. We created a 3D model within the context of elasticity with large distortions using a Neo-Hookean incompressible material model.[53] The residual swelling stimulus is represented by a spherical distortion field $\vec{F}_o = \alpha(\eta^3)\vec{I}$ where η^3 is the general coordinate normal to the midsurface (*i.e.* across the thickness). Shells are composed of two layers: in the swelling (green) layer, $\alpha(\eta^3) = \lambda_o$, and in the other (pink) layer, $\alpha(\eta^3) = 2 - \lambda_o$, where λ_o represents an inelastic stretching factor (see Fig. 6). This ensures that the conformal stretching factor $\Lambda_o \simeq 1$, as was found experimentally for residual swelling bilayers.[50] The constraints were modeled with Dirichlet boundary conditions imposed around a ring of radius R_c in each case, reflecting the experimental setup. Solving for the deformed shape while varying geometric parameters, we confirmed our experiments from Section 1 for rolled sheets, cylinders, and spheres.

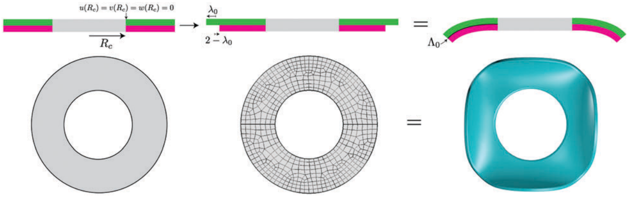

Fig. 6 Top: Schematics depicting the distortion field and boundary conditions applied in COMSOL to the bilayer geometry, and the resulting deformation. Bottom: Top-down images from simulations showing the geometry, mesh, and deformation.

A.4 Buckling dynamics

We know from ref. 50 that for the unconstrained rolled sheet ($\ell_p = 1$), the critical buckling curvature (normalized by the thickness) is

$$\kappa_b h = \sqrt{10 + 7\sqrt{2}}\left(\frac{h}{R}\right)^2. \tag{6}$$

We examine the effect of constraint on this value – our numerics allow us to extract the critical curvature required for buckling for various values of ℓ_p. This is shown in Fig. 7

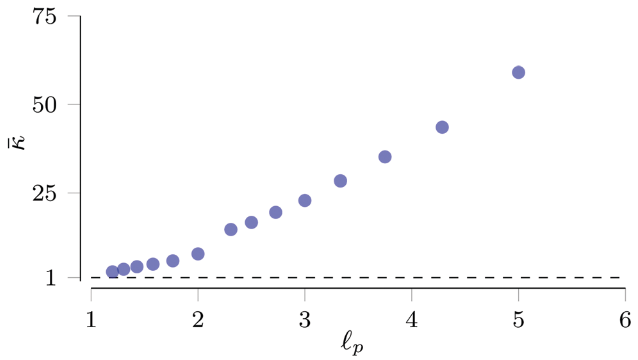

Fig. 7 The critical buckling curvature for rolled sheets increases with the extent of constraint, quantified by ℓ_p. $\bar{\kappa}$ is the ratio of the critical buckling curvature to that of the unconstrained case, from (6).

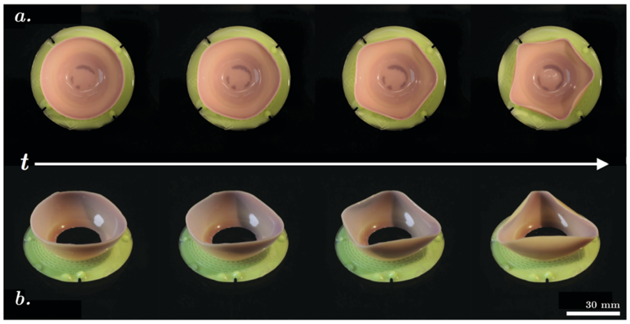

Fig. 8 Timelapse images of constrained swelling spherical segments. Time between photos is about 40 minutes. (a) As curvature develops, a spherical segment ($\ell \approx 2$) develops five increasingly curved lobes. (b) A different sample ($\ell \approx 1$) is unstable through the residual swelling process: at lower curvatures (earlier in the residual swelling process), four lobes emerge. As curvature continues to increase, the spherical segment settles on three lobes as its energy-minimizing configuration.

by $\bar{\kappa}$, which represents the ratio of the buckling curvature of the constrained structure over an unconstrained but otherwise geometrically identical sheet (according to (6)). We observe that the buckling curvature increases with ℓ_{p} or, in other words, that more constrained structures require more curvature to buckle.

Curvature continues to develop past the critical buckling point, and we generally observe that lobes become increasingly pronounced, as in Fig. 8a. However, when ℓ corresponds to an intermediate N value, the lobe-selection process can be unstable (Fig. 8b). A similar bistability between two mode numbers is seen in some shells after residual swelling is complete.

Acknowledgements

We are grateful to James Hanna for helpful discussions. LSM and DPH gratefully acknowledge the financial support from NSF through CMMI-1824882.

Notes and references

1 E. Cerda, *J. Biomech.*, 2005, **38**, 1598–1603.
2 J. B. Bard and J. Bard, *Morphogenesis: the cellular and molecular processes of developmental anatomy*, Cambridge University Press, 1992, vol. 23.
3 J. B. Bard and A. S. Ross, *Dev. Biol.*, 1982, **92**, 73–86.
4 J. B. Bard and A. S. Ross, *Dev. Biol.*, 1982, **92**, 87–96.
5 J. Dervaux and M. Ben Amar, *J. Mech. Phys. Solids*, 2011, **59**, 538–560.
6 J. Dervaux, Y. Couder, M.-A. Guedeau-Boudeville and M. B. Amar, *Phys. Rev. Lett.*, 2011, **107**, 018103.
7 M. Ben Amar and M. Wu, *EPL*, 2014, **108**, 38003–38007.
8 J. Dervaux, J. C. Magniez and A. Libchaber, *Interface Focus*, 2014, **4**, 20130051.
9 A. Goriely, *The Mathematics and Mechanics of Biological Growth*, Springer, 2017.
10 W. Yang, T. Fung, K. Chian and C. Chong, *J. Biomech.*, 2007, **40**, 481–490.
11 M. M. Lee and S. Chien, *Anat. Rec.*, 1979, **194**, 1–14.
12 X. Lu, J. Zhao and H. Gregersen, *J. Biomech.*, 2005, **38**, 417–426.
13 P. M. Reis, H. M. Jaeger and M. Van Hecke, *Extreme Mech. Lett.*, 2015, **5**, 25–29.
14 Y. Klein, E. Efrati and E. Sharon, *Science*, 2007, **315**, 1116–1120.
15 D. P. Holmes, M. Roché, T. Sinha and H. Stone, *Soft Matter*, 2011, **7**, 5188.
16 J. Kim, J. A. Hanna, M. Byun, C. D. Santangelo and R. C. Hayward, *Science*, 2012, **335**, 1201–1205.
17 J. Dervaux and M. B. Amar, *Annu. Rev. Condens. Matter Phys.*, 2012, **3**, 311–332.
18 A. Pandey and D. P. Holmes, *Soft Matter*, 2013, **9**, 5524.
19 Z. L. Wu, M. Moshe, J. Greener, H. Therien-Aubin, Z. Nie, E. Sharon and E. Kumacheva, *Nat. Commun.*, 2013, **4**, 1586–1587.
20 M. Pezzulla, G. P. Smith, P. Nardinocchi and D. P. Holmes, *Soft Matter*, 2016, **12**, 4435–4442.
21 M. Pezzulla, S. A. Shillig, P. Nardinocchi and D. P. Holmes, *Soft Matter*, 2015, **11**, 5812–5820.
22 M. Pezzulla, N. Stoop, M. P. Steranka, A. J. Bade and D. P. Holmes, *Phys. Rev. Lett.*, 2018, **120**, 048002.
23 T. Mora and A. Boudaoud, *Eur. Phys. J. E: Soft Matter Biol. Phys.*, 2006, **20**, 119–124.
24 S. J. DuPont, Jr, R. S. Cates, P. G. Stroot and R. Toomey, *Soft Matter*, 2010, **6**, 3876.
25 W. Barros, E. N. de Azevedo and M. Engelsberg, *Soft Matter*, 2012, **8**, 8511.
26 E. Efrati, E. Sharon and R. Kupferman, *J. Mech. Phys. Solids*, 2009, **57**, 762–775.
27 M. A. Dias, J. A. Hanna and C. D. Santangelo, *Phys. Rev. E: Stat., Nonlinear, Soft Matter Phys.*, 2011, **84**, 036603.
28 W. M. van Rees, E. Vouga and L. Mahadevan, *Proc. Natl. Acad. Sci.*, 2017, 201709025.
29 P. Domokos, G. Holmes and B. Royce, *J. Nonlinear Sci.*, 1997, **7**, 281–314.
30 P. Holmes, G. Domokos, J. Schmitt and I. Szeberényi, *Comput. Methods Appl. Mech. Eng.*, 1999, **170**, 175–207.
31 B. Roman and A. Pocheau, *EPL*, 1999, **46**, 602–608.
32 B. Roman and A. Pocheau, *J. Mech. Phys. Solids*, 2002, **50**, 2379–2401.
33 A. Pocheau and B. Roman, *Phys. D*, 2004, **192**, 161–186.
34 M. Ben Amar and Y. Pomeau, *Proc. R. Soc. London, Ser. A*, 1997, **453**, 729–755.
35 E. Cerda and L. Mahadevan, *Phys. Rev. Lett.*, 1998, **80**, 2358.
36 S. Chaeb, F. Melo and J.-C. Géminard, *Phys. Rev. Lett.*, 1998, **80**, 2354.
37 E. Cerda, S. Chaieb, F. Melo and L. Mahadevan, *Nature*, 1999, **401**, 46–49.
38 S. Chaieb, *J. Mech. Phys. Solids*, 2000, **48**, 565–579.
39 E. Cerda and L. Mahadevan, *Proc. R. Soc. London, Ser. A*, 2005, **461**, 671–700.
40 J. Hure, B. Roman and J. Bico, *Phys. Rev. Lett.*, 2012, **109**, 054302.
41 J. D. Paulsen, V. Démery, C. D. Santangelo, T. P. Russell, B. Davidovitch and N. Menon, *Nat. Mater.*, 2015, **14**, 1206.
42 A. Vaziri and L. Mahadevan, *Proc. Natl. Acad. Sci.*, 2008, **105**, 7913–7918.
43 A. Nasto, A. Ajdari, A. Lazarus, A. Vaziri and P. M. Reis, *Soft Matter*, 2013, **9**, 6796–6799.
44 D. Vella and B. Davidovitch, arXiv preprint arXiv:1804.03341, 2018.
45 J. D. Paulsen, arXiv preprint arXiv:1804.07425, 2018.
46 Z. Liu, W. Hong, Z. Suo, S. Swaddiwudhipong and Y. Zhang, *Comput. Mater. Sci.*, 2010, **49**, S60–S64.
47 L. Mahadevan, A. Vaziri and M. Das, *EPL*, 2007, **77**, 40003.
48 X. Jiang, M. Pezzulla, H. Shao, T. K. Ghosh and D. P. Holmes, *EPL*, 2018, **122**, 64003.
49 Y. Klein, E. Efrati and E. Sharon, *Science*, 2007, **315**, 1116–1120.
50 M. Pezzulla, N. Stoop, X. Jiang and D. P. Holmes, *Proc. R. Soc. London, Ser. A*, 2017, **473**, 20170087.
51 A. Lee, P. T. Brun, J. Marthelot, G. Balestra, F. Gallaire and P. M. Reis, *Nat. Commun.*, 2016, **7**, 11155.
52 J. Marthelot, P.-T. Brun, F. Lopez Jimenez and P. M. Reis, *APS Meeting Abstracts*, 2017, p. C15.010.
53 A. Lucantonio, P. Nardinocchi and M. Pezzulla, *Proc. R. Soc. London, Ser. A*, 2014, **470**, 20140467.